Solar Hydrogen Generation by a CdS-Au-TiO₂ Sandwich Nanorod Array Enhanced with Au Nanoparticle as Electron Relay and Plasmonic Photosensitizer

Jiangtian Li,[1,†] *Scott K. Cushing,*[1,2,†] *Peng Zheng,*[1] *Tess Senty,*[2] *Fanke Meng,*[1] *Alan D. Bristow,*[2] *Ayyakkannu Manivannan,*[3] and *Nianqiang Wu*[1,*]

[1]Department of Mechanical and Aerospace Engineering, West Virginia University, Morgantown, West Virginia 26506-6106, United States

[2]Department of Physics and Astronomy, West Virginia University, Morgantown, West Virginia 26506-6315, United States

[3]National Energy Technology Laboratory, U.S. Department of Energy, Morgantown, West Virginia, 26507, United States

*Corresponding author. Fax: +1-304-293-6258. Email: nick.wu@mail.wvu.edu.

†Indicates equal author contribution

Motivation, Explanation, and Implementation of Pump-Probe Inversion Analysis

It is difficult to interpret the effect of heterostructuring on the acceptor and donor lifetime, even if only the transfer out of the QD donor and not the complex dynamics of the trap states are considered. This can be seen in Figure S1, where a representative signal is shown for the CdS-TiO$_2$ samples pumped at 400 nm (exciting TiO$_2$ and CdS) and 480 nm (exciting CdS only) while being probed at the TiO$_2$ electron-trap state absorption. The decay dynamics of the TiO$_2$ and CdS alone pumped at 400 nm are shown for comparison. It is seen the initial transfer dynamics seem quicker in the heterostructure similar to CdS alone, while the long timescale transfer dynamics depend on whether carriers are excited in CdS alone or CdS and TiO$_2$.
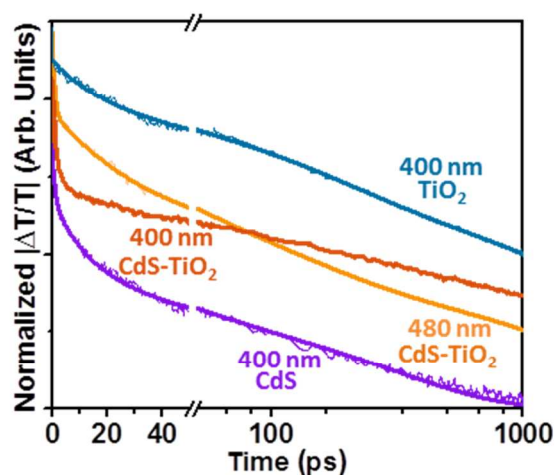
Figure S1. Transient-absorption signals for CdS, TiO$_2$ and CdS-TiO$_2$ at 400 nm and 480 nm pump wavelengths. The curves are shifted for comparison.

Traditionally, each decay curve is fit with 1 to 5 exponential terms and the relative lifetimes compared, giving a quantitative interpretation to the information gained by visual inspection. However, charge transfer lifetimes inferred from this fitting vary greatly depending on the number of exponentials used in the fit, the time scales measured, and how the average change in lifetime is defined.[S1-S8] Comparison of lifetimes is further encumbered when contributions from both the donor and acceptor exist at the measured probe wavelength, as evidenced in Figure S1. It is therefore difficult to conclude mechanistic details from the exponential fit, unless systematic

sample design is used to vary a structural parameter against which the change in lifetimes can be compared. Even in this case only the trend and not the absolute lifetimes are guaranteed quantitative.

The reason multiple exponential fits fail to accurately reflect dynamics is that the decay kinetics of a semiconductor are non-exponential by nature, with the dominant mechanisms such as Shockley-Read-Hall, radiative, surface recombination, and Auger scattering all depending explicitly on carrier density except in cases of low level injection. The different recombination mechanisms are illustrated in Figure S10 and Figure S11, along with their dependence on excited carrier density. The nonlinear dependence on the excited carrier density forbids simple exponential solutions of the rate equation. Although analytical solutions exist for nonlinear kinetics, the mechanism must be known before hand to select the appropriate model, as several possible models will often accurately describe the decays and be fit equally. Further, the common multiple exponential solution assumed for fitting cannot be obtained for a semiconductor treated as a two-level system even if the relaxation rate only depends linearly on carrier density. This is because additional linear rates just add inversely to the overall lifetime

$$\frac{\partial \Delta N}{\partial t} = -\frac{\Delta N}{\tau} \tag{S1}$$

with

$$\frac{1}{\tau} = \frac{1}{\tau_{rad}} + \frac{1}{\tau_{SRH}} + \frac{1}{\tau_{auger}} + \cdots \tag{S2}$$

assuming all lifetimes are independent of injected carrier density. This is only the case in low injection, with the actual governing rate equation resembling

$$\frac{\partial \Delta N}{\partial t} = -\frac{\Delta N}{\tau_{SRH}(\Delta N)} - \frac{\Delta N^2}{\tau_{RAD}} - \frac{\Delta N^3}{\tau_{AUGER}} - \cdots \tag{S3}$$

which no longer has a simple exponential solution.

Despite the indeterminate nature of multiple exponential fitting[S9,S10] and that a single exponential fit only holds in low-level injection,[S11-S13] using multiple exponential fits is prevalent because it is otherwise impossible to explain the relaxation data. The necessity of a multiple exponential fit for a single semiconductor can be seen for TiO_2 in Figure S1, which in-spite of

being dominated by SRH recombination with little Auger or radiative effects, still has a non-linear (or non-exponential) slope on a log plot. The non-exponential dynamics are even more pronounced in the CdS QD's, Figure S1. This is because the small volume of the QD means a single excited electron-hole pair translates into a charge density of $\sim 10^{22}$ to 10^{23} electrons/cm^3, which leads to Auger scattering dominating the initial recombination dynamics. The decay mechanism then evolve to radiative or SRH recombination as the charge carrier density decreases at longer timescales.[S14,S15]

The non-exponential dynamics are further magnified when the CdS and TiO$_2$ are combined in the heterostructure, Figure S1. Even if the two semiconductors had single exponential dynamics alone, the solution of the coupled first order rate equations is no longer single exponential, Figure S2a, as the charge transfer from the donor adds an exponential dependence to the rate equation of the acceptor. In a first order transfer model, the transfer reduces the lifetime of the donor by a constant rate but leads to non-single exponential dynamics for the acceptor. This allows the difference in average lifetime in the donor before and after coupling to be easily used to calculate the transfer rate, but disrupts knowledge of transfer dynamics once the carriers leave the donor. This explains the success of probing only the QD lifetime to determine the transfer time, but the difficulty in relating the determined transfer rate to the resulting acceptor dynamics. The first order coupled rate equation model predicts a rise in the acceptors decay as the donor relaxes. This trend can be found in organic dye–metal oxide or organic dye-organic dye charge transfer systems[S16,S17] but is generally absent in QD-metal oxide systems and organic dye-metal oxides with defects.[S18,S19] Therefore, while the transport out of the QD donor can be approximated by the change in average lifetime and even directly predicted by Marcus theory, the subsequent dynamics in the metal oxide acceptor cannot, leaving conflicting results about how charge transfer continues after the initial stage.

To overcome these issues, we have adapted an inversion analysis technique first proposed by Linnros[S11-S13] for single semiconductors using free carrier absorption (FCA). The multiple exponential fit has remained in wide use despite its limitations because it is otherwise difficult to

fit non-exponential dynamics: Not only must the coupled rate equations be solved, but the appropriate recombination mechanisms must be guessed and the unknown parameters found, leaving the original problem even more undetermined.[S10] However, instead of solving the rate equation the transient-absorption data can be transformed by taking the time derivative. This alters the transient-absorption data from the solution of the underlying rate equation back to the rate equation itself.

The form of the underlying rate equation can therefore be easily found experimentally by plotting the derivative of the transient absorption data verses the excited carrier density, as shown in Figure S2b for the coupled first order example. On a log-log plot, an exponential decay becomes a straight line with a shift above or below corresponding to a shorter or longer lifetime, respectively. Any curvature away from a straight line of slope one corresponds to non-exponential dynamics, with the order given by the slope. This gives the different recombination mechanisms unique forms, as shown in Figure S10, removing the ambiguity found in the decay data. Further, inverting the rate equation by dividing the derivative by the carrier density $\frac{d\Delta N}{dt}/\Delta N$ directly gives the instantaneous lifetime, allowing the relaxation constants to be determined without a fitting procedure. This can be seen by grouping the nonlinear dependence on carrier density into a carrier density dependent lifetime

$$-\frac{\partial \Delta N}{\partial t} = \Delta N \left(\frac{1}{\tau_{SRH}(\Delta N)} + \frac{1}{\tau_{RAD}(\Delta N)} + \frac{1}{\tau_{auger}(\Delta N)} \right) = \frac{\Delta N}{\tau(\Delta N)} \tag{S4}$$

so that

$$\frac{1}{\tau(\Delta N)} = -\frac{\frac{\partial \Delta N}{\partial t}}{\Delta N} . \tag{S5}$$

As shown in Figure S9, the instantaneous lifetime verses carrier density also helps uniquely show the recombination mechanism, with a traditional exponential solution again being a constant verses excited carrier density
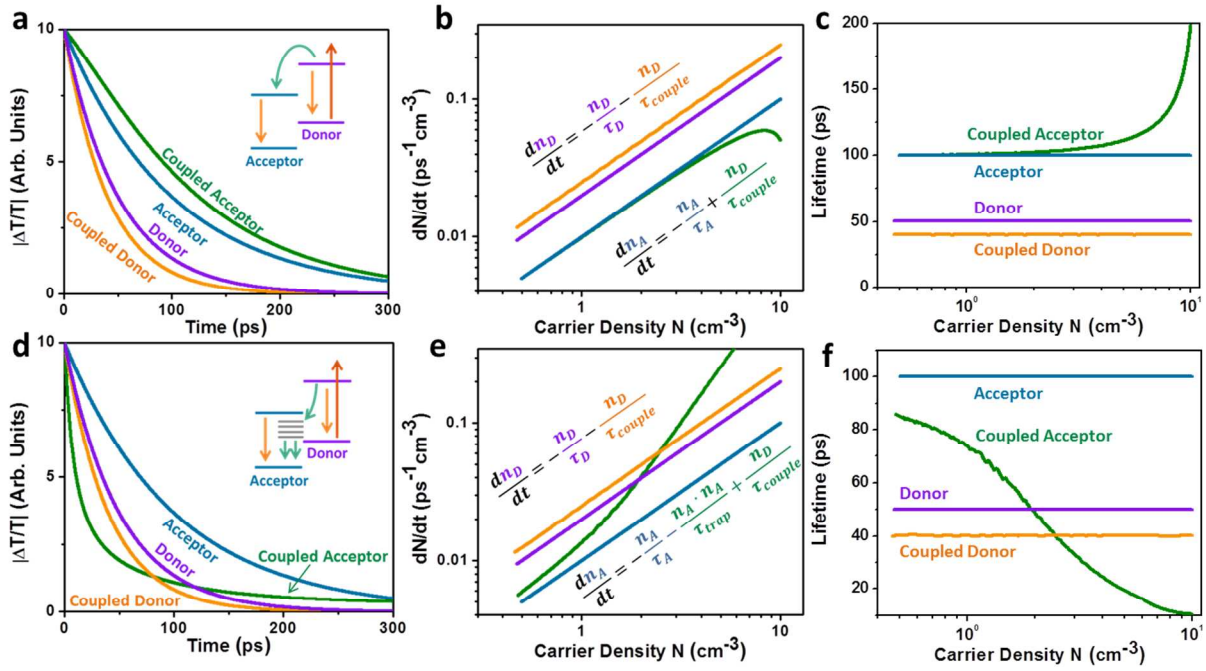
Figure S2. Modeled relaxation dynamics in heterostructures. The decay is shown for (a) a simple first order coupled rate equation and (d) a coupled rate equation with trap-state Auger recombination in the acceptor. By taking the derivative of the respective decay dynamics, (b) and (e), the form of the underlying rate equation is seen. In both cases the donor has an initially higher rate due to charge transfer. The charge transfer into the acceptor leads to a lower initial rate (b) for the first order coupled rate equation, but the addition of trap-state Auger scattering creates an initially higher relaxation rate. After charge transfer is complete the lifetime returns to that of the acceptor, as seen by the instantaneous lifetime in (c) and (f) found by inverting the rate equation of (b) and (e).

The utility of this technique in analyzing heterostructure is shown in Figure S2. If both donor and acceptor are measured, the inversion of the data transforms the pump probe signal into direct measurement of the coupled rate equation, regardless of the presence of non-exponential relaxation dynamics. The acceptor data in Figure S2a requires a multiple exponential fit despite the acceptor and donor having single exponential kinetics, with the fitted lifetimes of 40 ps and 115 ps differing from the true acceptor lifetime of 100 ps or the coupling time of 200 ps. The

inverted data in Figure S2b and S2c is seen to be much easier to interpret. After coupling, the donor lifetime of 50 ps is seen to be reduced by the coupling constant of 200 ps to 40 ps, directly mapping the donor's side of the rate equation (inset in Figure S2b). The acceptor rate is seen to be initially slower, corresponding to the exponential addition of carriers from the donor population as it decays. After the donor has decayed the lifetime of the acceptor returns to its own dynamics, illuminating the origin of the apparently multiple exponential dynamics in Figure S2a.

Procedure for Applying Inversion Analysis

The difficulty in experimentally applying the inversion analysis is smoothly taking the derivative of noisy data. Although several algorithms exist for smoothing the derivative, the results were found to tend to distort the curvature of the decay. Instead of smoothing the derivative, this problem was solved by utilizing the well-known ability of an over-parameterized multi-exponential decay to fit the transient absorption data and act as a filter. The inversion analysis therefore becomes as simple as performing the standard multi-exponential analysis, then taking the derivative of the result and inverting the absorption. As long as the data is completely fit, the derivative destroys the multi-exponential assumption and gives the underlying rate equation. The inversion is achieved by first transforming the transient absorption into a carrier density[S11-S13]

$$\frac{\Delta A}{A} = \frac{I_0 \exp(-(\alpha_{probe}+\sigma\Delta N)d)-I_0 \exp(-\alpha_{probe}d)}{I_0 \exp(-\alpha_{probe}d)} = \exp(-\sigma\Delta Nd) - 1 \tag{S6}$$

so that

$$\Delta N = -\frac{1}{\sigma d}\ln(1 \pm \left(\frac{\Delta A}{A}\right)) \tag{S7}$$

where the $\pm$ is used to ensure the excited carrier density is positive whether the signal is a bleach or an excited state absorption. The absorption cross section σ acts as a calibration between the number of excited carriers in the sample, found by[S11-S13]

$$N_{exc} = \frac{I_0}{\hbar\omega} \cdot \frac{\alpha_{pump}(1-R)^2 \exp(-\alpha_{pump}d)}{1-R^2 \exp(-\alpha_{pump}d)} \approx \frac{I_0 \cdot \alpha_{pump}}{\hbar\omega} \tag{S8}$$

where $N_{exc} = \Delta N$ and the measured increase in transient absorption signal is

$$\frac{\Delta A}{A} = \exp(-\sigma \Delta N d) - 1 \approx \pm \sigma N_{exc} d \ . \tag{S9}$$

The cross section can therefore be found by the slope of the maximum of the transient absorption verses several excitation intensities. In these equations, $\pm$ depends on if the signal is an excited state absorption or bleach, I_0 is the incident flux in J/cm^2, α is the absorption coefficient in cm^{-1}, $\hbar \omega$ is the energy of the pump, R is the reflection coefficient, d is the sample thickness in cm, and N_{exc} is the number of excited carriers per cm^3. After this is complete, the data can be fit with an arbitrary number of exponentials so the decay is completely represented, *i. e.* the exponentials are simply acting as a filter of the noise. The derivative of the data can then be taken, comparing to the unfiltered (or unfit) derivative to ensure accuracy.

In the data reported, the plots were shifted slightly for comparison by multiplying the derivative of the carrier density and carrier density by a constant. This is equivalent to changing the effective absorption cross section and does not change the dynamics, especially in the case of a constant lifetime like that measured for the donors. The fitting coefficients given in Figure S14 and Table S1 were calculated without shifting the data for comparison. The small shifts are purely to aide in visualizing the difference in high and low carrier dynamics between the different pump wavelengths and heterostructures.
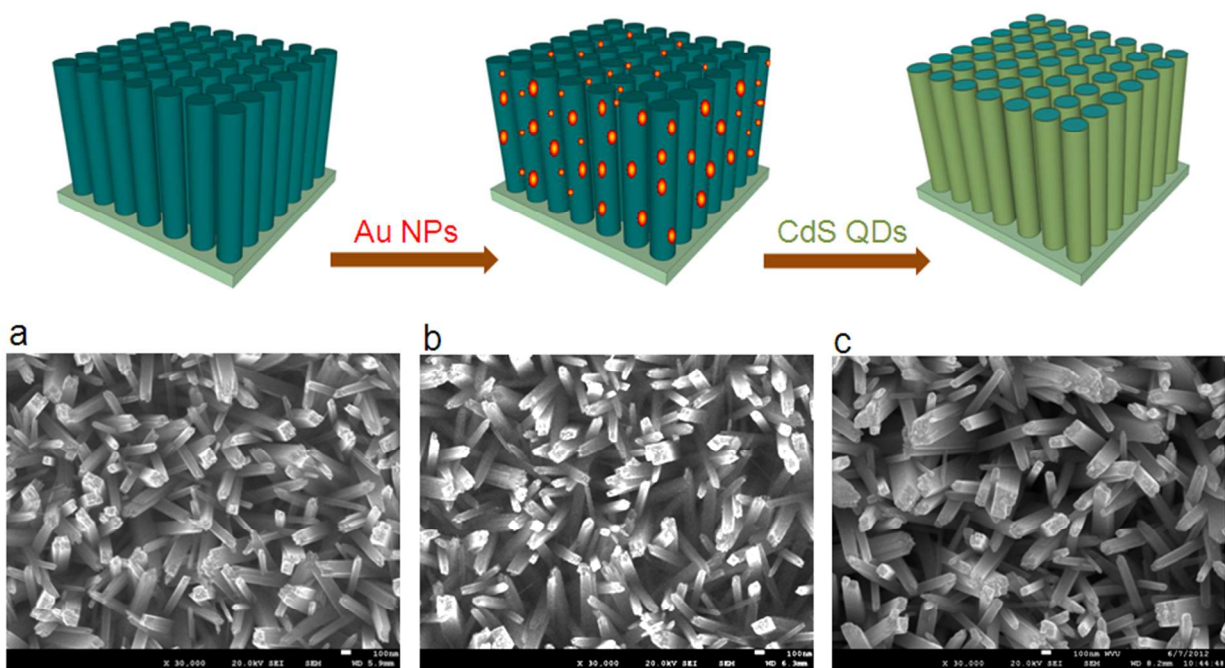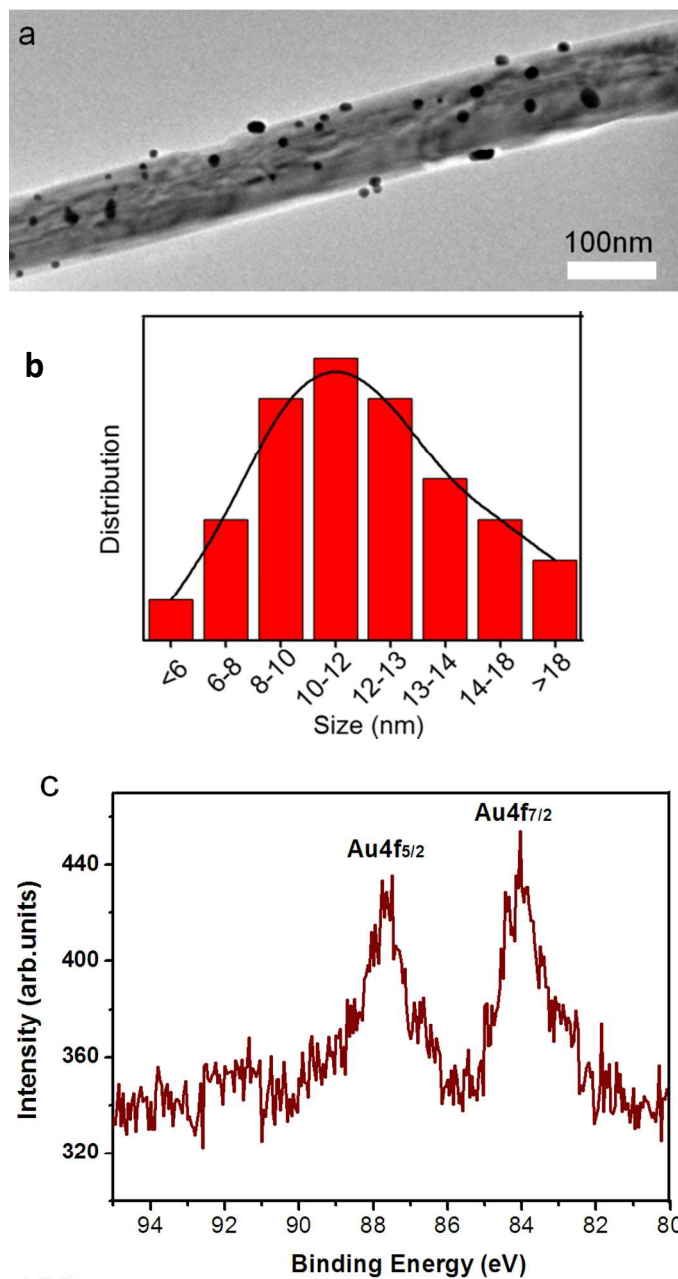
Figure S3. Scheme for synthesis of the sandwich CdS-Au-TiO$_2$ nanorod array; and SEM images of (a) Au-TiO$_2$, (b) and (c) CdS-Au-TiO$_2$.
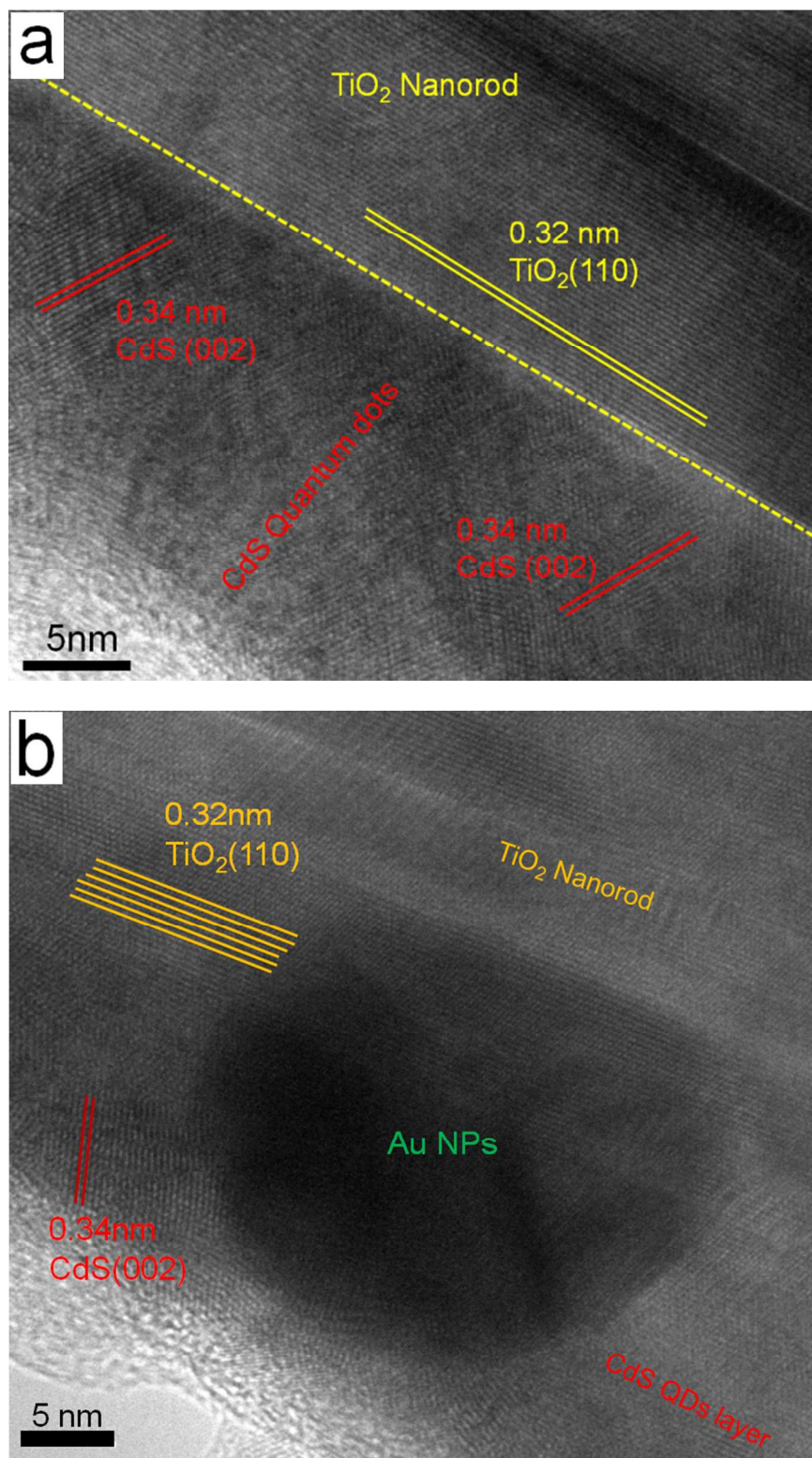
Figure S4A. HRTEM images obtained from CdS-TiO$_2$ (a) and CdS-Au-TiO$_2$ (b), respectively.

Figure S4B. (a) SEM image of Au nanoparticles distribution on the TiO$_2$ nanorod with an average size of 11.5±3nm; (b) A histogram showing the size distribution of Au nanoparticles; (c) Au 4f   XPS spectrum showing the metallic Au nanoparticles.
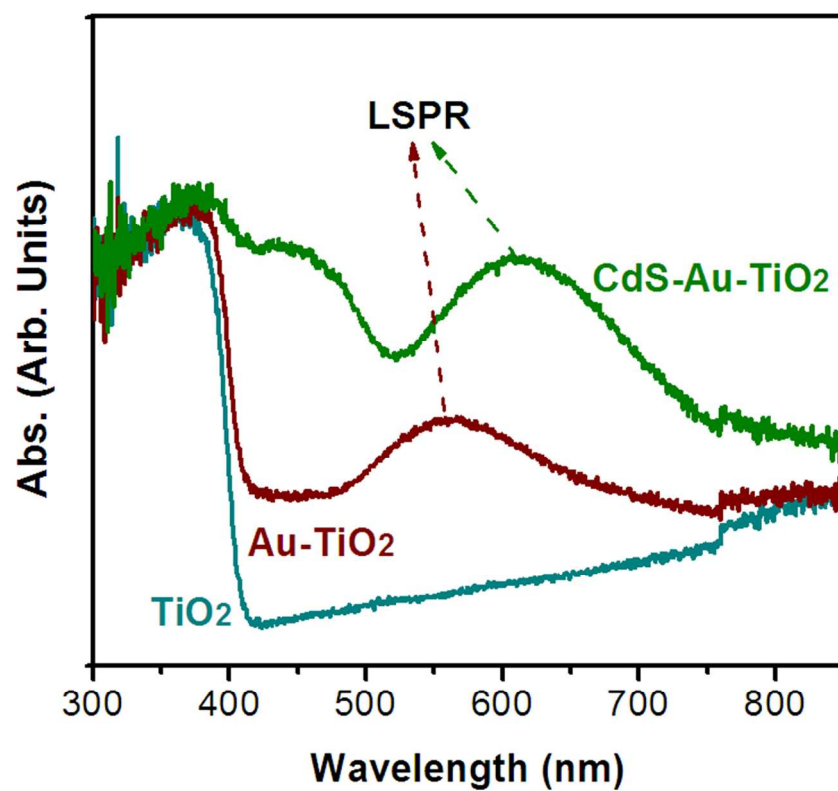
**Figure S5.** UV-Visible absorption spectra of TiO_2 and the Au-TiO_2 heterostructure. An absorption band centered at ~550 nm was observed due to the LSPR of Au nanoparticles.
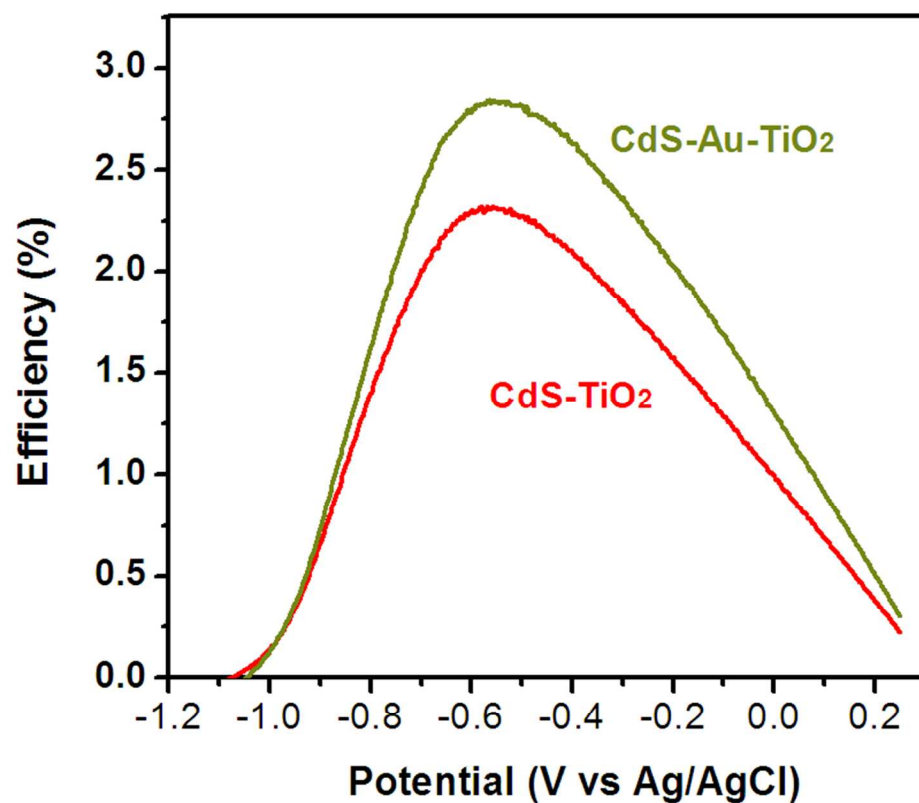
Figure S6. Solar-to-chemical energy conversion efficiency of the PECs with the CdS-TiO$_2$ and the CdS-Au-TiO$_2$ as the photoanodes under the irradiation of the full spectrum of simulated solar light of 100 mW/cm^2.
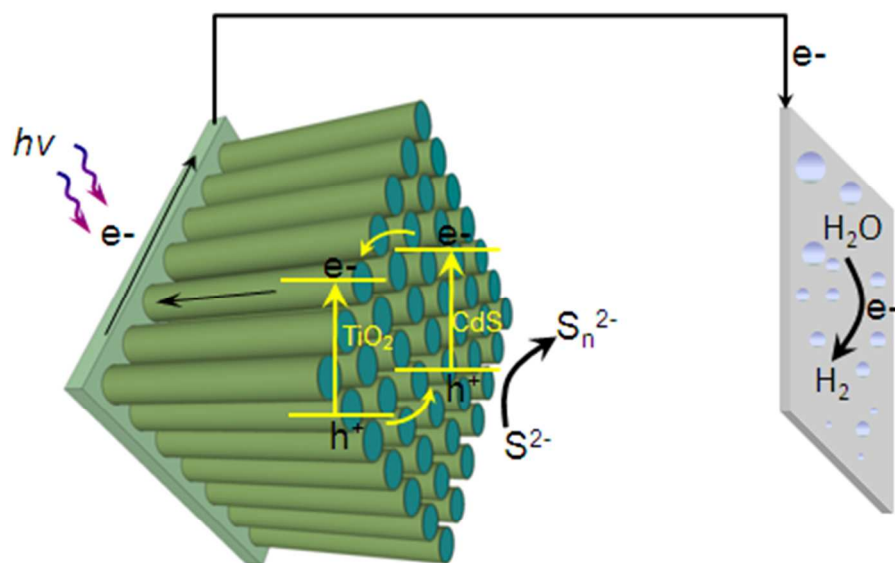
Figure S7. Scheme of the PEC with the CdS-Au-TiO$_2$ nanorod array as the photoanode and Pt as the counter electrode. An aqueous solution containing 0.25 M Na$_2$S and 0.35M Na$_2$SO$_3$ was employed as the electrolyte. When the CdS is excited with visible light, electrons in the conduction band of CdS are injected into the conduction band of TiO$_2$. The photo-generated electrons flow towards the FTO while holes are scavenged by S^{2-} to produce polysulfide ions [S$_n^{2-}$].
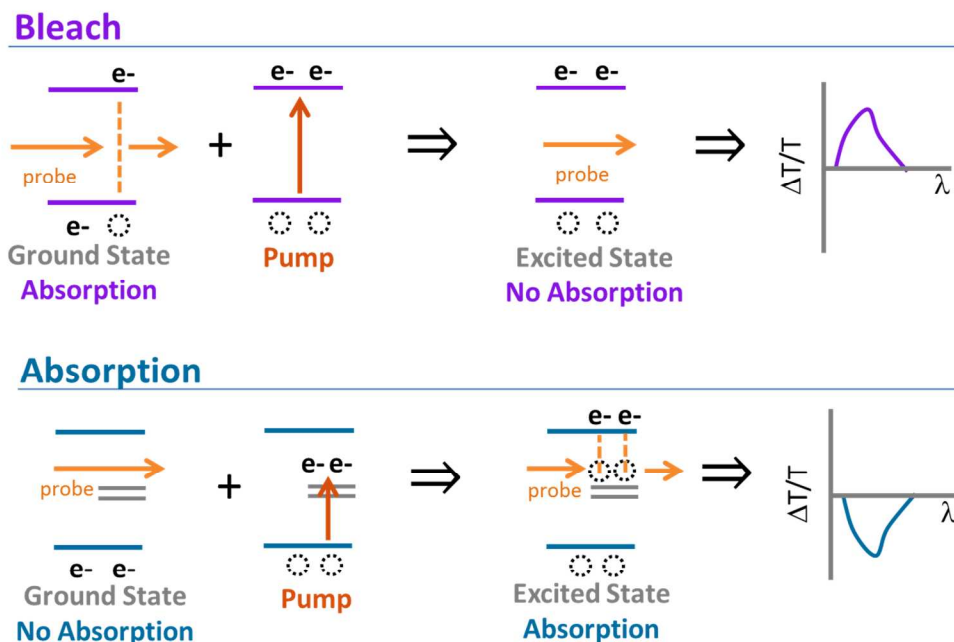
Figure S8. Sign of signal in transient absorption. If a semiconductor is probed near the band edge or an absorption band, after excitation, less carriers will be present. This leads to a decrease in the overall absorption of the probe, and the differential transient absorption signal is negative (or the differential transmission is positive). This is known as a bleach. The bleach has a spectral form given by the product of the density of states and quasi-Fermi level under excitation, meaning the bleach is usually similar in position to the ground state absorption. If the probed state is unoccupied before excitation and the excitation wavelength pumps carriers directly into the band, the resulting differential absorption will be positive because more light will be absorbed after excitation (or the differential transmission will be negative). If the state is unoccupied before excitation, the excited state absorption can differ from the ground state absorption, leading to the measurement of absorption at wavelengths shorter than the band edge.
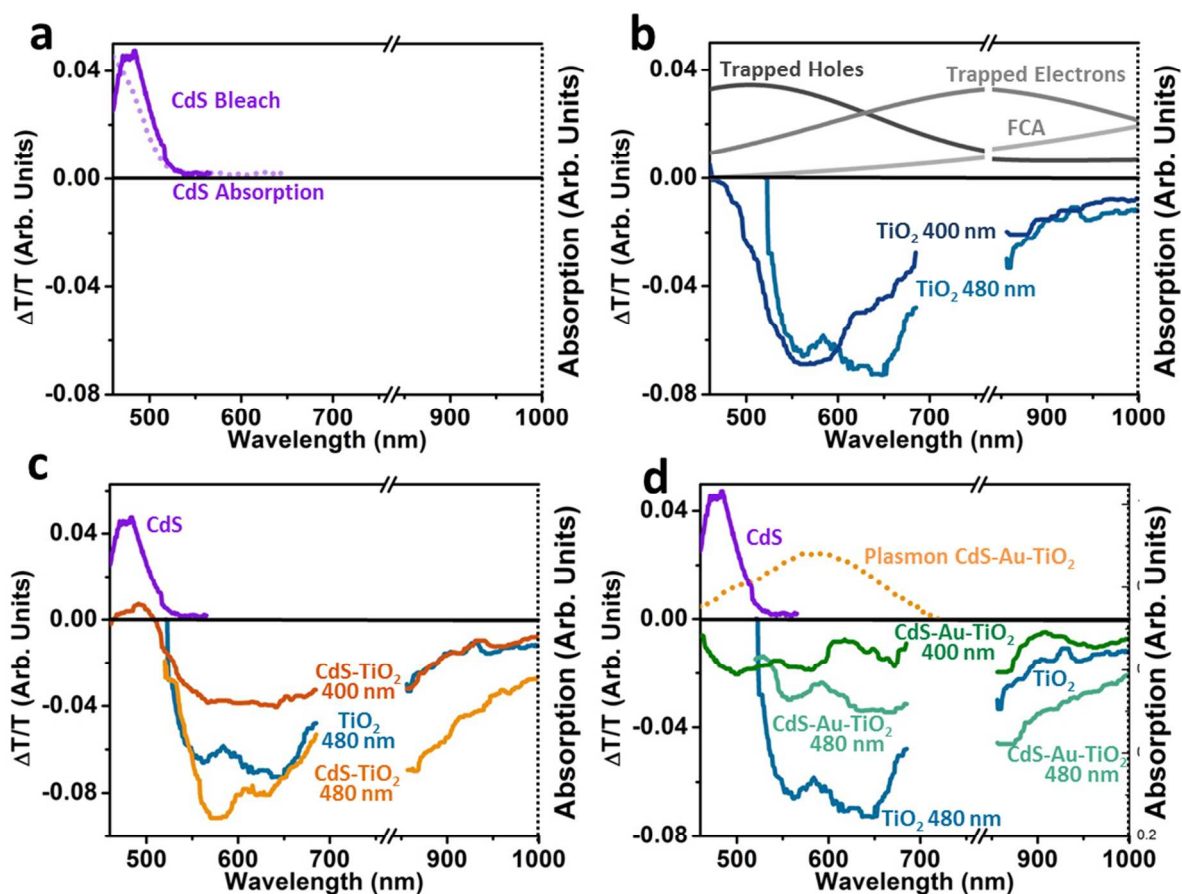
Figure S9. Full spectrum transient absorption at 20 ps after excitation. (a) Transient absorption for CdS alone pumped at 400 nm, showing the bleach of the exciton. (b) The transient absorption for TiO_2 shows excited state absorption bands below the band edge. These correspond to trapped holes, trapped electrons, and free carrier absorption as outlined in Ref. S20. (c) In the CdS-TiO_2 heterostructure the TiO_2 excited state absorption and CdS bleach is separate, allowing the observation of both electron and hole transfer pathways. At 480 nm excitation the pump wavelength is too close to the white light spectrum edge, so the CdS bleach cannot be observed. (d) The CdS bleach cannot be observed in the CdS-Au-TiO_2, and instead an excited state absorption is seen in the same spectral region. This is consistent with the Au mixing with the CdS states as previously reported.[S21-30]
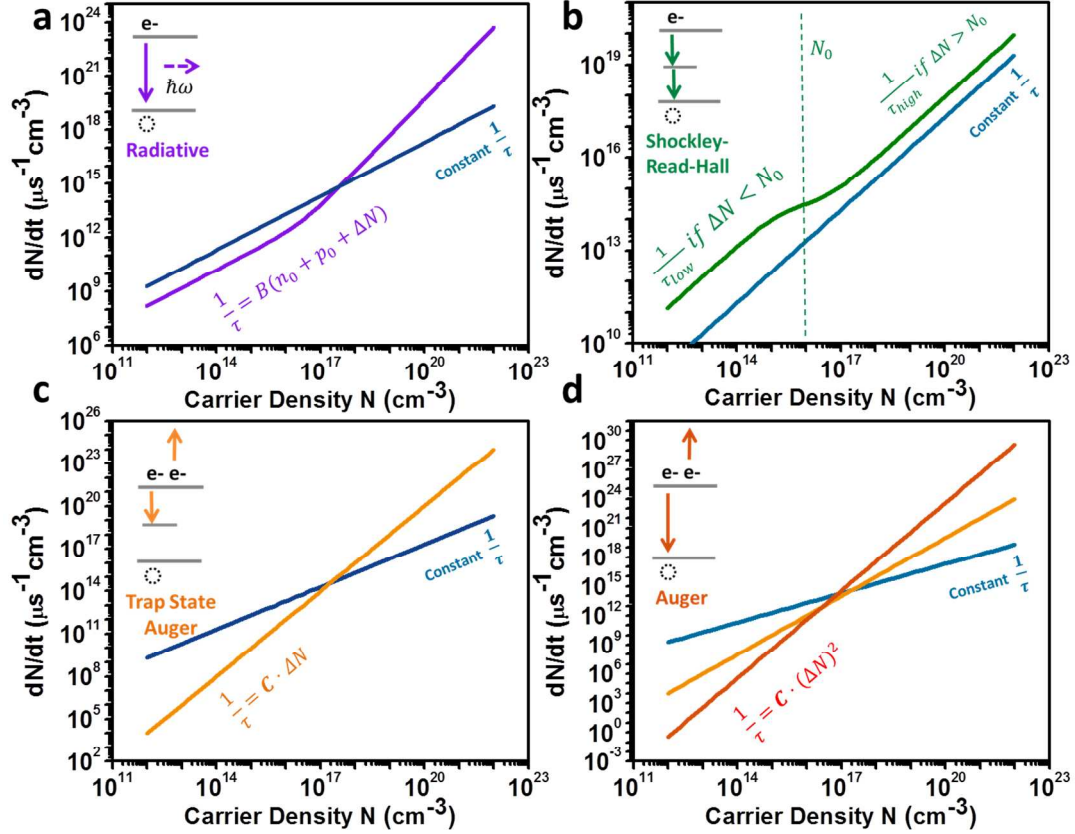
Figure S10. Nonlinear nature of relaxation mechanisms in semiconductors. A schematic diagram, mathematical form, and a constant lifetime curve (exponential decay) is shown in each graph for comparison. (a) At low carrier injection levels radiative relaxation which occurs by the emission of a photon is first order, or linear on the slope of rate verses carrier density. At higher injection levels the radiative relaxation becomes second order. (b) Shockley-Read-Hall recombination occurs through mid-gap trap states. SRH transitions between two first order relaxation rates depending on the excited carrier density relative to the doping level. The transition between these two areas depends on the position of the trap states in the band gap, and several other parameters as shown in more detail in Ref S11-S13. (c) Trap-state based Auger scattering is a second order process that occurs by an electron relaxing to a trap state by giving its energy to a second electron. The rate has a slope of 2 on a log-log plot. (d) Auger recombination is a third order process where an electron and hole recombine by giving energy to a third electron, leading to a slope of three on a log-log plot. In all cases the intercept of the log-log plot gives the rate coefficient of the mechanism. The given curves are based off parameters given in Ref. S13
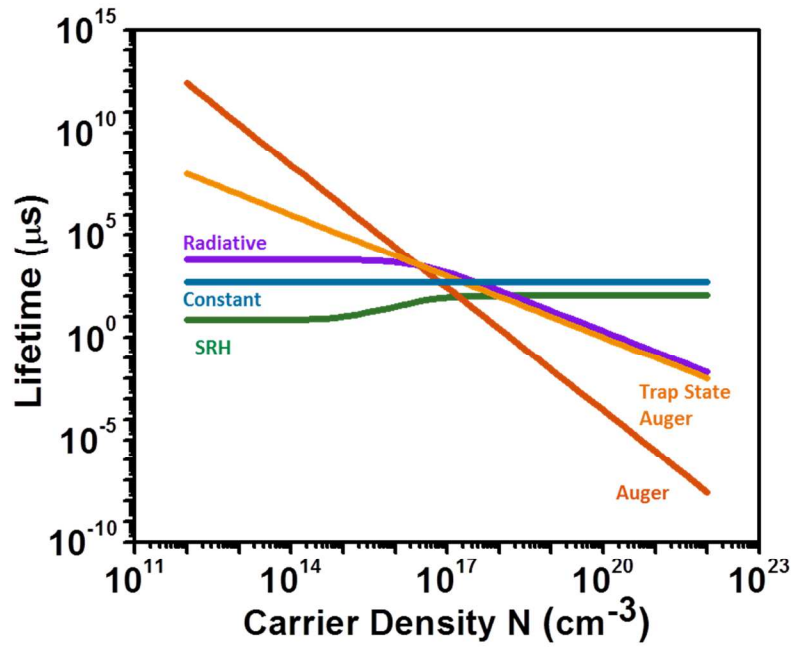
Figure S11. Instantaneous lifetime for each of the recombination mechanisms shown in Figure S10. The curves are obtained by dividing the carrier density by the derivative of the carrier density verses time, inverting the rate equation. The given curves are based off parameters given in Ref. S13, showing how nonlinear relaxation terms dominate during high carrier injection, which correspond to short time scales in transient absorption. On long time scales the carrier dynamics become constant.
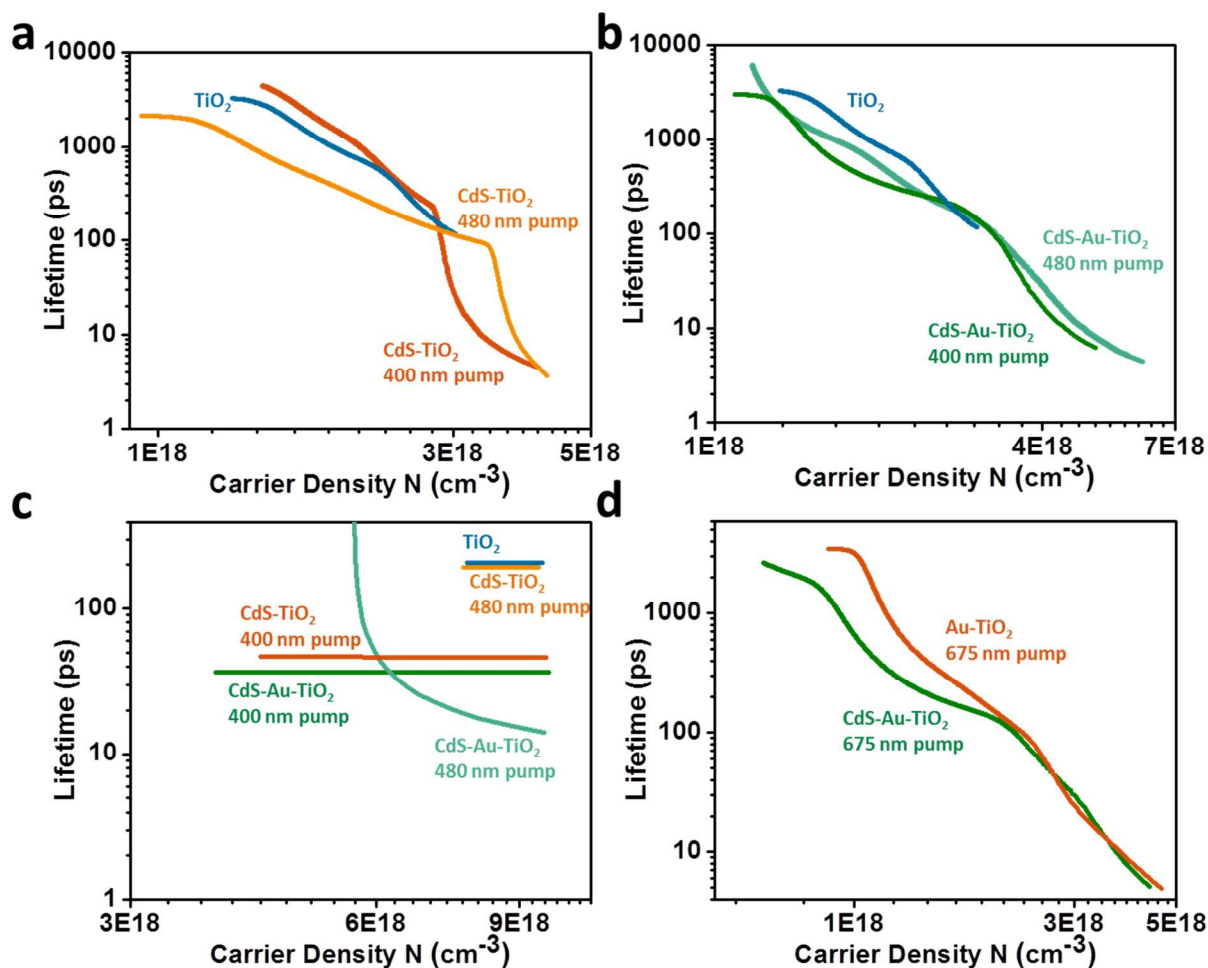
Figure S12. Instantaneous lifetime verses carrier density for band edge excitation in (a) electron trap states in CdS-TiO$_2$, (b) electron trap states in CdS-Au-TiO$_2$, (c) hole trap states for CdS-TiO$_2$ and CdS-Au-TiO$_2$, and (d) electron trap states in Au-TiO$_2$ and CdS-Au-TiO$_2$ when the LSPR is excited.
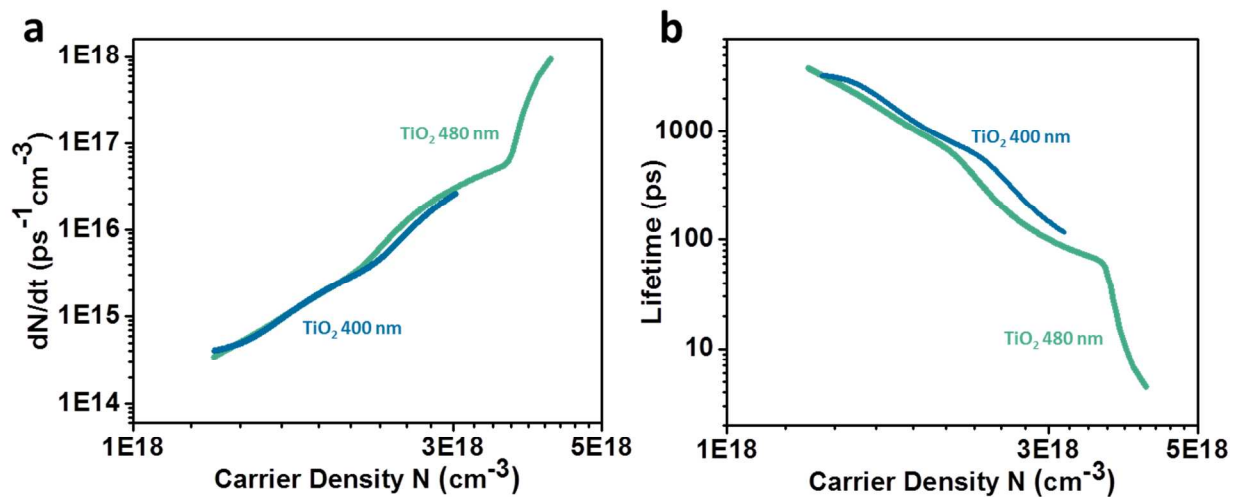
Figure S13. Instantaneous lifetime and rate verses carrier density for band edge excitation and direct pumping in TiO$_2$, showing that trap-state Auger dynamics dominate when the trap states are directly pumped.
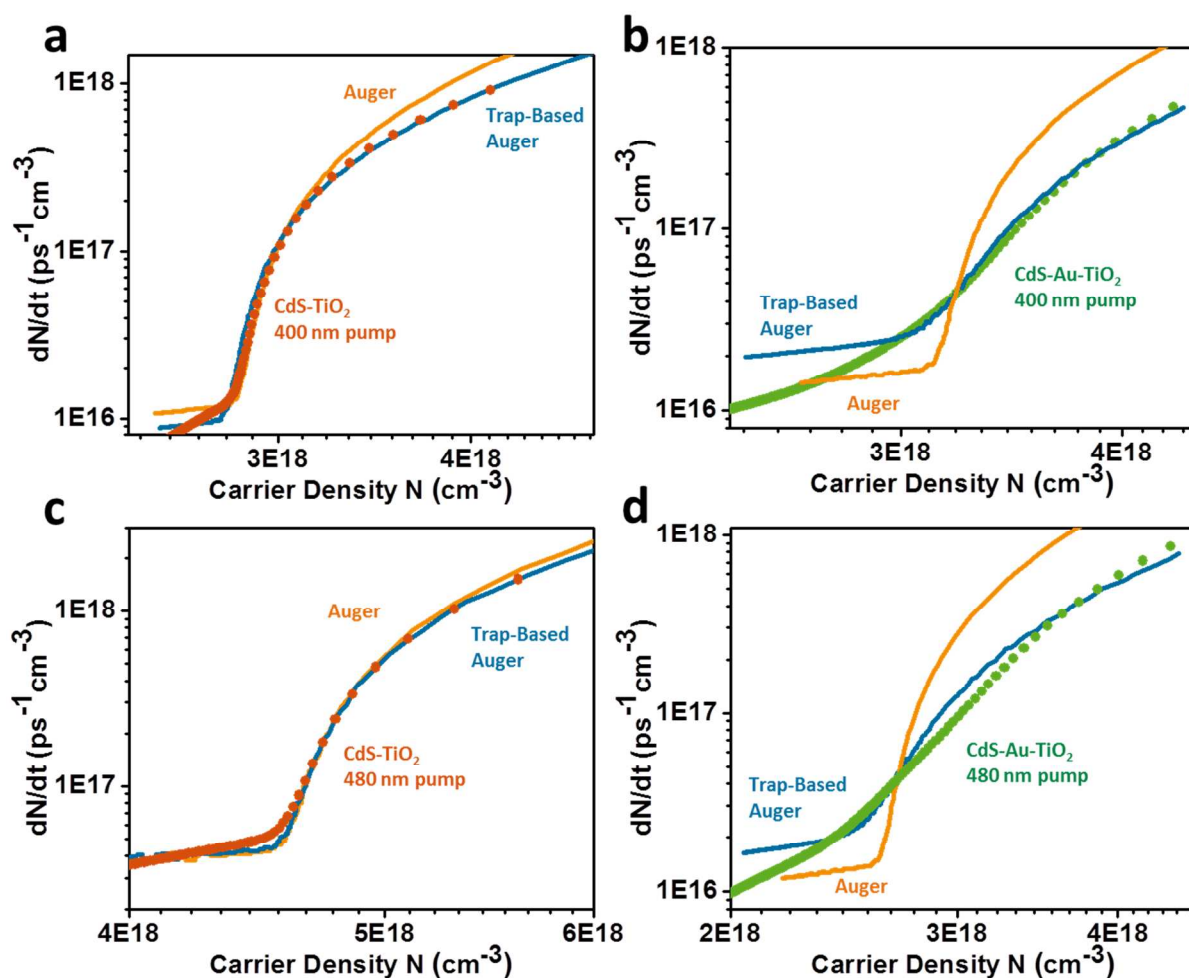
Figure S14. Fitting the trap-state Auger coupled rate equation to the decay dynamics in the TiO_2 electron trap states for CdS-TiO_2 under (a) 400 nm and (c) 480 nm excitation and CdS-Au-TiO_2 under (b) 400 nm and (d) 480 nm excitation, which correspond to excitation of the CdS and TiO_2 or CdS alone, respectively. In all cases Auger scattering, a third order process, can not fit the data, only a second order process like trap state Auger scattering fits. The CdS-Au-TiO_2 can not be completely fit using the simple model due to the different trap state filling and dynamics caused by the Au-semiconductor interaction.[S21-29] The fit parameters are in Table S1. The curves in Figure S14 are not shifted for comparison to ensure accuracy of the fit parameters (see Procedure for Applying Inversion Analysis at the beginning of the Supporting Information).
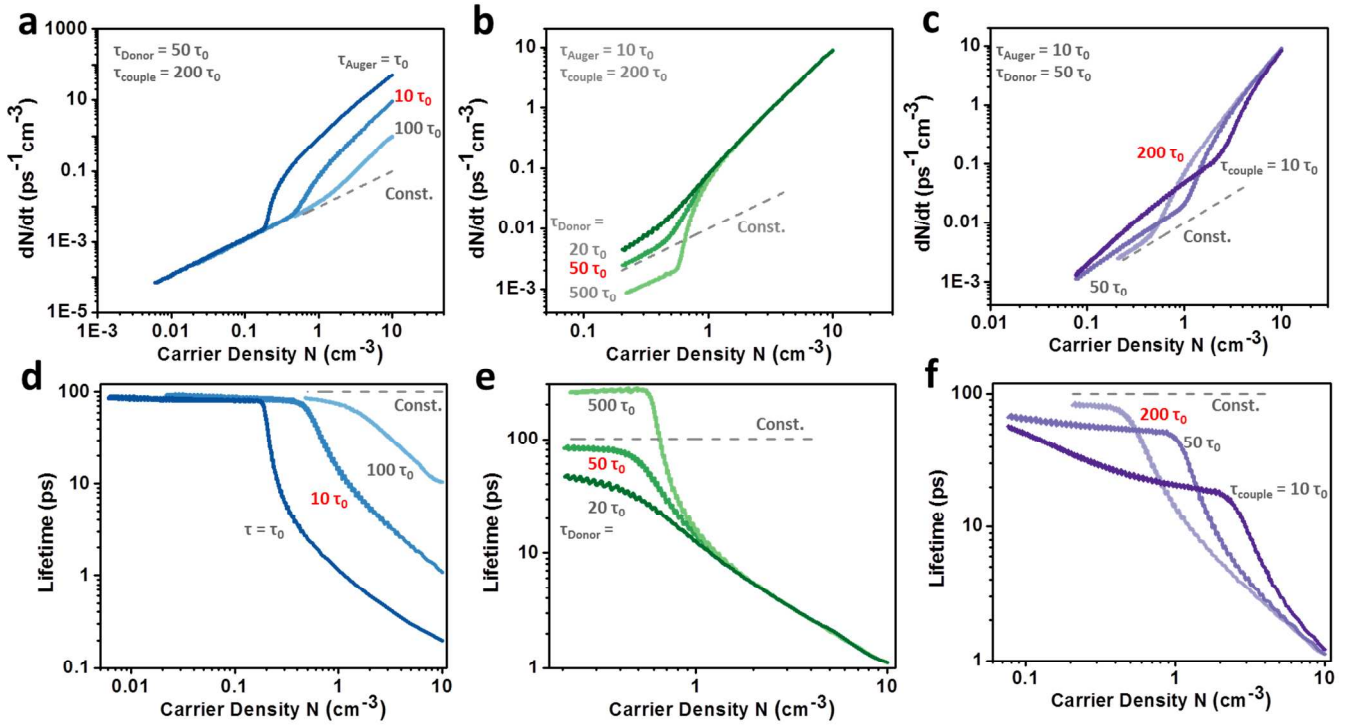
Figure S15. The trap state Auger coupled rate equation is given by

$$\frac{dN_{Acceptor}}{dt} = -\frac{N_{Acceptor} * N_{Acceptor}}{\tau_{Auger}} + \frac{N_{Donor}}{\tau_{couple}}$$

$$\frac{dN_{Donor}}{dt} = -\frac{N_{Donor}}{\tau_{Donor}} - \frac{N_{Donor}}{\tau_{couple}}$$

The effect of modulating (a) the trap state Auger scattering rate, (b) the effective donor lifetime which describes the lifetime as seen by the acceptor, and (c) the charge transfer time are shown. The corresponding change in instantaneous lifetime is shown in (d) through (f). It is seen that the trap state scattering rate modulates the initial curvature, the effective donor lifetime changes the rate after transfer, and the coupling time determines the range over which carriers are transferred.
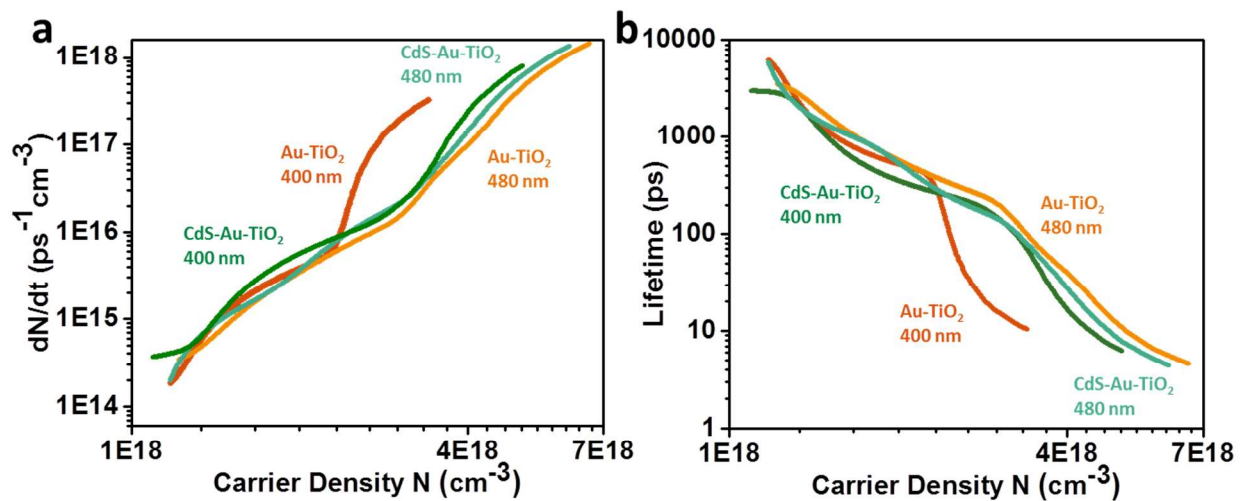
Figure S16. Instantaneous lifetime and rate verses carrier density for Au-TiO$_2$ and CdS-Au-TiO$_2$ for 400 nm and 480 nm excitation. The dynamics are seen to be modified from pure TiO$_2$ in all cases, with heterostructuring further changing the transfer times. This is consistent with Au acting as an electron sink and shuttle, as well as modifying the interface states.[S21-30]

Table S1. Fitting parameters for transfer model in Figure S14.

Sample	Pump	Trap-State Auger Rate ($cm^3 ps^{-1}$)	Couple Lifetime (ps)	Donor Lifetime (ps)
CdS-TiO$_2$	400 nm	5.3×10^{-20}	200	500
	480 nm	1.7×10^{-19}	70	200
CdS-Au-TiO$_2$	400 nm	5.9×10^{-20}	70	500
	480 nm	6.5×10^{-20}	70	500

Table S2. Change in short time scale lifetime of the donors with heterostructuring. The 480 nm excited, trapped hole TiO$_2$ lifetime had decaying and growing components. The 400 nm CdS electrons in CdS-Au-TiO$_2$ did not have a bleach at the CdS peak due to the mixing between Au and CdS.

Probe	Sample	Pump	Lifetime (ps)	Transfer Time (ps)
Trapped Holes	TiO$_2$	400 nm	214	-----
		480 nm	193	-----
	CdS-TiO$_2$	400 nm	47	60
		480 nm	195	~0
	CdS-Au-TiO$_2$	400 nm	38	46
		480 nm	N/A	N/A
CdS Electrons	CdS	400 nm	73	---
	CdS-TiO$_2$	400 nm	36	71
	CdS-Au-TiO$_2$	400 nm	N/A	N/A

References

(S1)   Cánovas, E.; Moll, P.; Jensen, S. A.; Gao, Y.; Houtepen, A. J.; Siebbeles, L. D. A.; Kinge, S.; Bonn, M. *Nano Lett.* **2011**, *11*, 5234–5239.

(S2)   Tisdale, W. A.; Williams, K. J.; Timp, B. A.; Norris, D. J.; Aydil, E. S.; Zhu, X.-Y. *Science* **2010**, *328*, 1543–1547.

(S3)   Shen, Q.; Ayuzawa, Y.; Katayama, K.; Sawada, T.; Toyoda, T. *Appl. Phys. Lett.* **2010**, *97*, 263113.

(S4)   Blackburn, J. L.; Selmarten, D. C.; Nozik, A. J. *J. Phys. Chem. B* **2003**, *107*, 14154–14157.

(S5)   Blackburn, J. L.; Selmarten, D. C.; Ellingson, R. J.; Jones, M.; Micic, O.; Nozik, A. J. *J. Phys. Chem. B* **2005**, *109*, 2625–2631.

(S6)   Tvrdy, K.; Frantsuzov, P. A.; Kamat, P. V. *Proc. Natl. Acad. Sci. U. S. A.* **2011**, *108*, 29–34.

(S7)   Jin, S.; Lian, T. *Nano Lett.* **2009**, *9*, 2448–2454.

(S8)   Pernik, D.; Tvrdy, K. *J. Phys. Chem. C* **2011**, *115*, 13511–13519.

(S9)   Osborne, M.; Smyth, G. *SIAM J SCI STAT COMP* **1991**, *16*, 119–138.

(S10)   BONNEAU, J. R.; ZUBERBUHLER, A. *Pure & Appl. Chem.* **1997**, *69*, 979–992.

(S11)   Linnros, J. *J. Appl. Phys.* **1998**, *84*, 275.

(S12)   Linnros, J. *J. Appl. Phys.* **1998**, *84*, 284.

(S13)   Grivickas, V.; Linnros, J. In *Charecterization of Materials*; John Wiley and Sons, Inc., 2012; p. 658.

(S14)   Klimov, V.; McBranch, D.; Leatherdale, C.; Bawendi, M. *Phys. Rev. B* **1999**, *60*, 13740–13749.

(S15)   Qu, Y.; Ji, W.; Zheng, Y.; Ying, J. Y. *Appl. Phys. Lett.* **2007**, *90*, 133112.

(S16)   Sakata, T.; Hashimoto, K.; Hiramoto, M. *J. Phys. Chem.* **1990**, *94*, 3040–3045.

(S17)   Stockwell, D.; Yang, Y.; Huang, J.; Anfuso, C.; Huag, Z.; Lian, T. *J. Phys. Chem. C* **2010**, *114*, 6560–6566.

(S18)   Hao, E.; Anderson, N. *J. Phys. Chem. B* **2002**, *106*, 10191–10198.

(S19)   Bisquert, J.; Zaban, A.; Salvador, P. *J. Phys. Chem. B* **2002**, *106*, 8774–8782.

(S20)   Yoshihara, T.; Katoh, R.; Furube, A. *J. Phys. Chem. B* **2004**, 3817–3823.

(S21)   Hirakawa, T.; Kamat, P. *Langmuir* **2004**, *20*, 15–17.

(S22)   Subramanian, V.; Wolf, E. E.; Kamat, P. V. *J. Am. Chem. Soc.* **2004**, *126*, 4943–4950.

(S23)   Choi, H.; Chen, W.; Kamat, P. *ACS Nano* **2012**, *6*, 4418–4427.

(S24)   Khon, E.; Mereshchenko, A.; Tarnovsky, A. N.; Acharya, K.; Klinkova, A.; Hewa-Kasakarage, N. N.; Nemitz, I.; Zamkov, M. *Nano Lett.* **2011**, *11*, 1792–1799.

(S25)   Kobayashi, Y.; Nonoguchi, Y.; Wang, L.; Kawai, T.; Tamai, N. *J. Phys. Chem. Lett.* **2012**, *3*, 1111–1116.

(S26)   Dreaden, E. C.; Neretina, S.; Qian, W.; El-Sayed, M. a.; Hughes, R. a.; Preston, J. S.; Mascher, P. *J. Phys. Chem. C* **2011**, *115*, 5578–5583.

(S27)   Zhang, W.; Govorov, A.; Bryant, G. *Phys. Rev. Lett.* **2006**, *97*, 146804.

(S28)   Artuso, R. D.; Bryant, G. W. *Phys. Rev. B* **2010**, *82*, 195419.

(S29)   Mongin, D.; Shaviv, E.; Maioli, P.; Crut, A.; Banin, U.; Del Fatti, N.; Vallée, F. *ACS Nano* **2012**, *6*, 7034–7043.

(S30)   Wu, K.; Rodríguez-Córdoba, W. E.; Yang, Y.; Lian, T. *Nano Lett.* **2013**, *13*, 5255–5263.